

Full length article

Integrated modelling of a 6061-T6 weld joint: From microstructure to mechanical properties



D. Bardel ^{a, b, c}, M. Fontaine ^d, T. Chaise ^a, M. Perez ^{b, *}, D. Nelias ^a, F. Bourlier ^c, J. Garnier ^e

^a Université de Lyon, INSA-Lyon, LaMCoS UMR CNRS 5259, F69621 Villeurbanne, France

^b Université de Lyon, INSA-Lyon, MATEIS UMR CNRS 5510, F69621 Villeurbanne, France

^c AREVA NP, 69456 LYON Cedex 06, France

^d ESI Group Le Récamier 70, Rue Robert 69458, Lyon Cedex 06, France

^e CEA, DEN, DMN, SRMA, F-91191 Gif-sur-Yvette, France

ARTICLE INFO

Article history:

Received 1 February 2016

Received in revised form

2 June 2016

Accepted 7 June 2016

Available online 14 July 2016

Keywords:

Welding

Age hardening

Aluminium alloy

Finite element analysis

Digital image correlation

ABSTRACT

Welding can highly modify the mechanical properties of materials due to the extreme thermal solicitations applied. For precipitation hardened materials, such as aluminium alloy 6xxx, a welding operation implies a modification of the microstructural state and, consequently, of the mechanical properties, both phenomena being highly nonlinear. The purpose of this paper is to propose a methodology to predict the post-welding mechanical properties of a welded joint. For this, three models are coupled: (i) a thermal finite element model of the welded structure that allows the prediction of the material's thermal history at every point; (ii) a precipitation model to predict the microstructural state in the joint using the thermal history; and (iii) a mechanical model to link the microstructural state to the mechanical properties, i.e. hardness, yield limit and hardening. A coupling between these models and a finite element commercial code is then performed to predict the precipitation state and mechanical properties of a 6xxx-T6 aluminium alloy after welding. To validate this methodology a tensile test is performed on a specimen extracted from a 6061-T6 welded plate. Using Digital Image Correlation, the in-plane strain fields across the weld are measured and compared with the finite element simulation of the tensile test, thereby providing good prediction.

© 2016 Acta Materialia Inc. Published by Elsevier Ltd. All rights reserved.

1. Introduction

6xxx series aluminium alloys are widely used (especially in the T6 state) for several applications, thanks to their good combination of formability, damage tolerance and specific strength [1,2] due to a large density of β'' hardening precipitates [3]. However, to assemble parts to produce industrial structures, welding is often used. Welded joint properties are strongly dependent on the post-welding microstructural state [4–7]. This high temperature heat treatment leads to very significant changes in the microstructural state of the material within the Molten Zone (MZ) and the Heat Affected Zone (HAZ): precipitates may grow, shrink, dissolve and/or coarsen, and the mechanical properties of the initial T6 state are lost [7–9].

The integrated modelling of heterogeneous structures has

greatly progressed within the last decade (see e.g. the review of Simar et al. [7]). To account for the heterogeneous aspect of the weld, Nielsen et al. [6] and later Puydt et al. [10] machined micro-tensile samples at various positions around the melted zone. Local mechanical properties were later introduced within a Finite Element (FE) framework and compared successfully to the local deformation field obtained by Digital Image Correlation (DIC). However, this approach requires an accurate identification of the position of the weld and each FE calculation is therefore dependant on the welding conditions (geometry, welding energy, steady-state profile, boundary conditions, etc.), restraining the predictive ability of the whole method.

To overcome these limitations, one has to predict the material's microstructural evolution (e.g. precipitation state) at each FE integration point, for which a coupling between FE and the microstructural model is needed. The first coupling approach, which can provide microstructural information in each integration point, consists of using phenomenological microstructural approaches, such as the so-called isokinetic model proposed by Myhr et al. [11].

* Corresponding author.

E-mail addresses: Didier.Bardel@insa-lyon.fr (D. Bardel), michel.perez@insa-lyon.fr (M. Perez).

This method was later used and coupled with mechanical models to provide a good evaluation of hardness profiles (see Hirose et al. [12]) or residual deformations after welding [13]. Nevertheless, these models oversimplify the physical mechanisms (nucleation/growth-dissolution and coarsening) [5] and avoid the extension to more complex microstructural-mechanical studies that require the knowledge of precipitate size distribution [7,14]. Hence, to get a complete distribution of precipitates but also to capture it in an adequate manner, even for rapid temperature fluctuations [15], a KWN-type (Kampmann-Wagner-Numerical [16]) model has to be coupled with finite element simulations.

In a previous work [13], an instrumented fusion line experiment was performed by Electron Beam Welding (EBW) in order to calibrate a thermal FE model using the equivalent source approach [17,18]. Conversely the recent studies in literature, a full coupling between FE simulations and the microstructural model is employed to offer a continuum of material properties across the weld, adapted to any kind of 3D transient thermal process. In this paper, an integrated approach, composed of a physical microstructural yield stress and a semi-phenomenologic work hardening model calibrated on anisothermal treatments, is proposed and coupled with the commercial FE software SYSWELD® [19]. This permits the mechanical behaviour of a heterogeneous weld (in terms of the precipitation state) to be addressed. Its goal is to accurately describe fields of the precipitation state, the yield strength and the work hardening resulting from highly non-isothermal treatments. Afterwards, a numerical tensile test is performed on a transverse section extracted from the FE plate where the thermal history is known at each point. The numerical results obtained from this integrated approach will be compared with to the experimental strain fields provided by the DIC method on the heterogeneous structure.

To present this coupling, this paper is divided into three parts:

- Experimental: To introduce (i) the welding device used to calibrate the FE model [13] and to provide the cross-weld specimens, (ii) the tensile tests performed after anisothermal representative heat treatments [9], and (iii) the DIC experiment performed on the heterogeneous structure.
- Modelling: A multiclass precipitation model [9] is presented as well as its coupling with a new semi-phenomenological elasto-plastic approach.
- Simulation: The thermal FE model is applied on a 6061-T6 blank which contains the mechanical specimen used for cross-weld mechanical simulation. Thus, the numerical Green-Lagrange strain fields will be compared with the experimental ones.

2. Experimental investigations

2.1. Fusion line treatment for thermal FE calibration

The first objective of these experiments is to get thermal histories to calibrate a FE thermal simulation of welding and to provide an heterogeneous sample, in terms of precipitation state, to perform a transverse-weld tensile test.

An instrumented Electron Beam (EB) fusion line was performed on a 6061-T6 plate where several K-type thermocouples were fixed. The EB welding device used in this study has a power of 5.47 kW and the relative velocity of the EB source is set to 0.45 m/min. To get a full penetration of the fusion line, a thickness of 20 mm (Z axis in Fig. 1) was chosen for the plate, the other dimensions being 180×200 mm (180 mm is in the fusion line direction, see X axis on the macrography in Fig. 1). This plate (its chemical composition is given in Table 1) has been extracted by machining (well lubricated

and with low velocity to decrease heat generation [20] and thus the impact on the microstructure) of the upper and lower surfaces from a 30 mm thickness cold rolled aluminium plate, to minimise the potential surface texture due to the cold roll process [21].

To reproduce the thermal field encountered during the process, the thermocouple histories and macrographies of the molten zone were used to calibrate a conical volumetric moving heat source. This methodology will not be described (see Ref. [13]) here. Fig. 1 represents the result of the thermal FE simulation and the comparison with one macrography of the middle section of the plate.

2.2. Hardness measurements

To characterise the post-welding mechanical properties of the weld joint, the Vickers hardness was measured. A semiautomatic microhardness Buehler OmniMet HMS machine was used in the central layer of the welded plate. A 0.3 kg load (applied during 10 s) was chosen in order to obtain small footprints compared with the molten zone size: the diagonal of the footprint for the base material was of the order of $70 \mu\text{m}$ and spacing between measures of about 0.35 mm.

In order to have an accurate characterisation of the fusion line, it was decided to conduct 9 cross lines in the thickness with a step of 0.4 mm in the HAZ and 2 mm beyond. The measurements were performed on a welded plate which was kept cold (in a freezer) after fusion line and air cooling in order to minimise the natural ageing effects, which are not accounted for in this study.

The obtained hardness map and two 1D hardness profiles are presented in the next section and confronted with numerical ones.

2.3. Cross-weld tensile test and Digital Image Correlation

To improve the mechanical characterisation of our heterogeneous structure, a tensile test was performed on the weld joint and

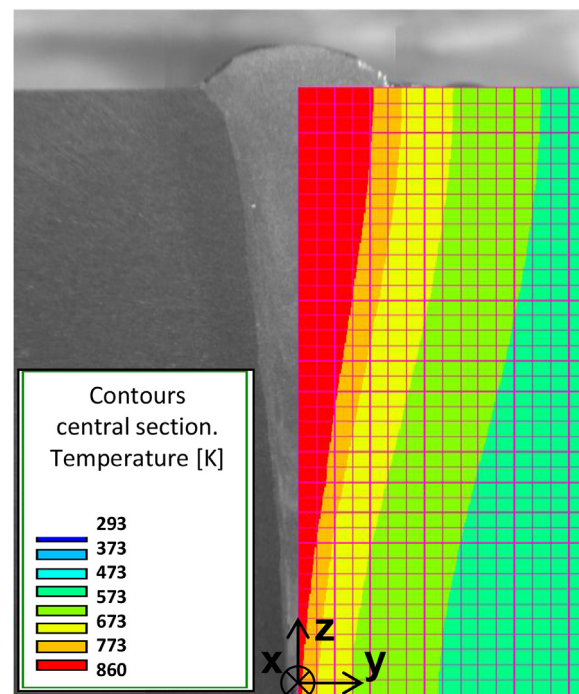


Fig. 1. Representation of the mid section of the plate and confrontation between the macrography (left) and numerical results from the calibration presented in Ref. [13]. These thermal results will be used as input for the metallurgical FE simulations.

Table 1

Chemical composition of the 6061 aluminium alloy used for the fusion line experiments.

	Mg	Si	Cu	Fe	Cr	Mn	Oth.
wt%	1.02	0.75	0.25	0.45	0.05	0.06	0.09
at.%	1.14	0.72	0.11	0.22	0.03	0.03	0.04

analysed by Digital Image Correlation (DIC). The central section of the welded plate (cf. Figs. 1 and 8) was extracted by electrical discharge machining to get the geometry of the tensile specimen (20 × 200 mm and 4 mm thickness). To permit a DIC measurement, a fine speckle pattern undercoat of mat white paint with black spray over it was applied. One face was painted and, for optimum detection, the specimen was lit uniformly. To obtain good accuracy, a CCD camera with 16 million pixels (4872 × 3248) was used, associated with an AF Micro-Nikkor objective (focal distance 200 mm).

The specimen was deposited between the auto-lock jaws of a Zwick tensile/compressive (capacity 100 kN) machine and then the stretcher was moved at a 0.2 mm/min velocity. The photos were recorded every 2 s during the tensile test thanks to the VicSnap software linked to the testXpertII machine hardware. Although strength was measured, the resulting stresses will not be considered in view of the non-uniformity of the strain field (Fig. 3). The experimental results and set-up are shown in Fig. 2.

The DIC treatment was performed thanks to the Icasoft software developed at INSA Lyon [22] from the undeformed state to the onset of fracture. The pattern of the DIC was square with a size of about 0.4 mm. The in-plane Green-Lagrange (E11, E22 and E12) strain fields are represented in Fig. 3 (pattern size equal to 20 pixels) for the last picture before rupture (displacement 2.2 mm). This state was followed by a localisation of the E11 and E22 Green-Lagrange strains in the molten zone whereas the maximum shear strain were located between the molten and the heat affected zone. Despite a high shearing at the interface between the molten and the heat affected zones, cracking was initiated at porosities on the foot of the weld joint (these porosities occur by gravity during

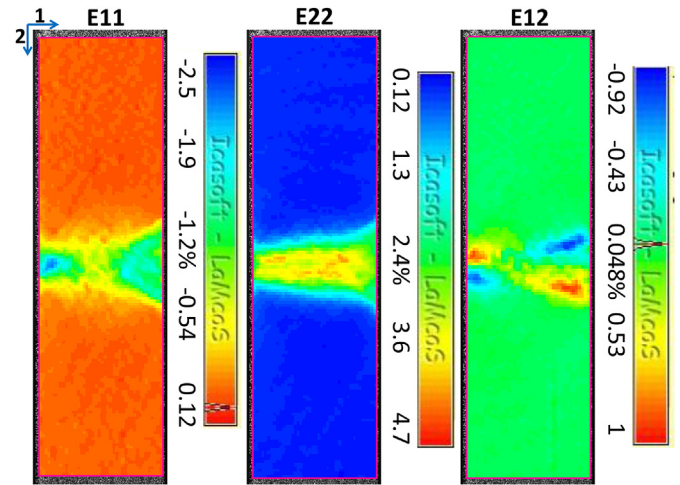


Fig. 3. Strain results provided by the DIC software for the last picture before crack initiation (cf. speckle in Fig. 2). The corresponding displacement is 2.2 mm.

welding when the plate is put horizontally [13]). This crack is initiated after 664 s for a jaw displacement of 2.21 mm (corresponding force is 16.1 kN).

2.4. Tensile test after anisothermal treatment

In order to calibrate a coupled microstructural-mechanical model for welding applications, tensile tests were performed after anisothermal heat treatments, as in Ref. [9]. These tests were conducted thanks to a homemade Joule device mounted on a MTS-809 tensile machine (100 kN load cell). To mimic thermal cycles occurring in the Heat Affected Zone (HAZ), controlled transient heat treatment were realised. These treatments are composed of a heating stage (constant heating rate) up to a Maximum Temperature (mt), followed by a cooling stage (natural cooling, like in a weld). In order to study the effects of both heating rate (τ) and Maximum Temperature (mt), two types of cycles were performed:

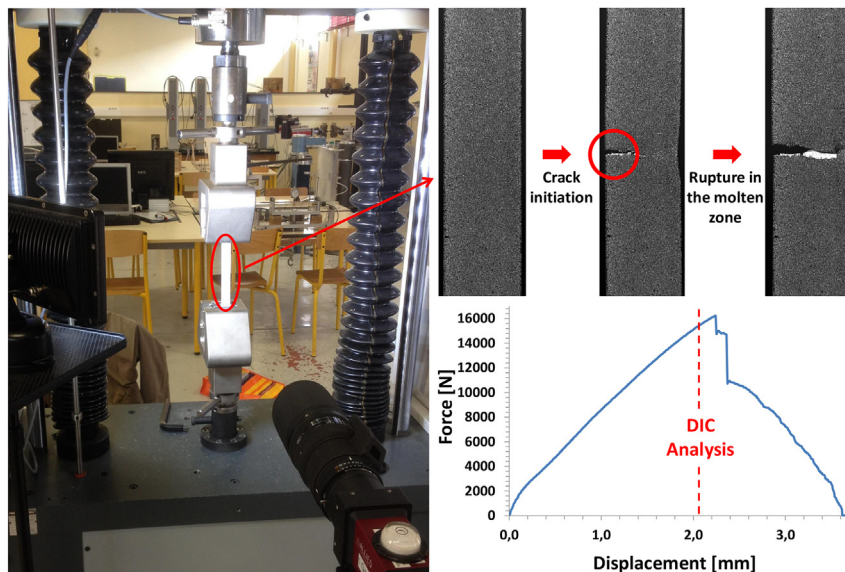


Fig. 2. Measuring device used for the cross-weld tensile test, representation of the force-displacement curve and three representative images of the test performed.

- At fixed heating rate (15 °C/s) and maximum temperature from 200 °C to 560 °C were reached,
- At fixed maximum temperature (400 °C), heating rates from 0.5 °C/s to 200 °C/s were performed.

These thermal cycles, similar to the ones presented in Refs. [9], are typical of thermal cycles occurring in a HAZ [13], and are assumed to be sufficiently representative of the process, to calibrate metallurgical models for these applications.

All the tensile tests, conducted at room temperature after transient heat treatment, are shown in Fig. 5 together with an Armstrong-Frederick fitting (see details in the next section). It was found that the thermal loading considerably influenced the mechanical properties of the specimens. Indeed, the 0.2% yield stress decreased from 280 MPa for the T6 state to 70 MPa when a maximum temperature (mt) of 500–560 °C was reached. For a similar Maximum Temperature, the lower the heating rate the worse the mechanical properties. These effects are associated with the dissolution and coarsening of the hardening precipitates during the anisothermal treatments [9].

3. Modelling

3.1. Modelling strategy

In this section, a semi-phenomenologic approach is proposed to reproduce the elasto-plastic behaviour observed during the tensile test at room temperature (Fig. 5) after the transient heat treatments. This model is then used to reproduce the hardness map (Fig. 11) and a tensile cross-weld test (Fig. 3). It includes a recently developed precipitation-yield stress model used to provide an initial distribution of precipitates in each element of the mesh [9]. Then, the initial yield stress of the alloy is provided as a function of the heat treatment at each integration point. In the last part of this section, this physical precipitation-yield stress approach will be coupled to a semi-phenomenological work hardening model calibrated on anisothermal tensile tests and written as a function of the precipitation hardening. Precipitation and proposed elasto-plastic models are finally implemented in a FE software and help provide, for our thermal FE simulation of welding [13] (Fig. 8), the microstructural state and the mechanical behaviour of the alloy at each integration point.

In this study, a weak coupling between the thermal and the mechanical simulation was used. This hypothesis was chosen because it is assumed that the distortions are small and the mechanical loading does not affect the thermal properties.

Next, a numerical tensile test on the weld joint was performed to reproduce the cross-weld tensile test. A confrontation between Green-Lagrange strain field (E) from DIC and FE is finally presented

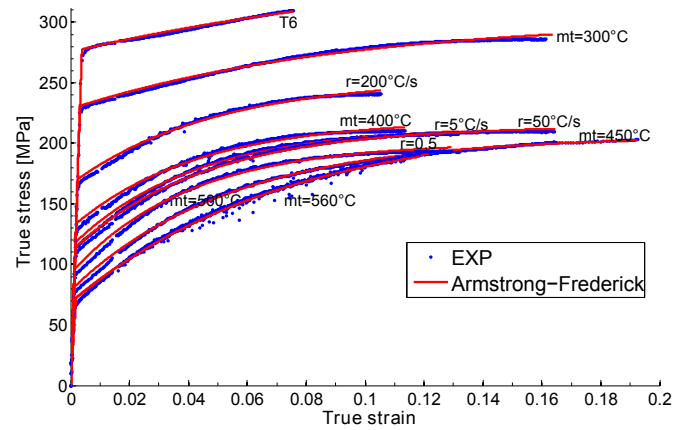


Fig. 5. Confrontation between experimental tensile tests (EXP) and an Armstrong-Frederick fitting. Each curve is representative of a specific anisothermal heat treatment: for various Maximum Temperatures (mt) and heating rates (r).

to show the accuracy of this approach and to validate the predicted results.

3.2. Precipitation modelling

The distribution of precipitates can be simulated in each element of the mesh thanks to a recent implementation of a KWN model for $\beta''-\beta'$ ($\text{Mg}_5\text{Si}_6-\text{Mg}_9\text{Si}_5$) hardening rods detailed in Bardel et al. [9]. This multi-class model, well adapted for anisothermal heat treatment [15], consists of three concurrent processes: the nucleation, growth and coarsening of precipitates. This sequence is run for each element to provide the number density and the radius of each rod in the particule size distribution.

The nucleation rate of the class 'i' (dN_i/dt) is described by the commonly accepted form proposed:

$$\frac{dN_i}{dt} = N_0 Z \beta^* \exp\left(\frac{-\Delta G^*}{k_B T}\right) \left(1 - \exp\left(\frac{-t}{\tau}\right)\right) \quad (1)$$

where the shape-dependant parameters are Z , β^* , ΔG^* : the Zeldovich factor, the condensation rate and the thermodynamic barrier for nucleation. The shape-independent constants (N_0 , τ) are the number of sites for nucleation and the incubation time [9]. The integration of eq. (1), thanks to an adaptive time step [23], provides the number density N_i of rod precipitates nucleating a radius r_{kBT}^* :

$$r_{kBT}^* = -\frac{2\gamma_p}{\Delta g} \frac{2\xi}{3\xi - 2} + \sqrt{\frac{k_B T}{4\gamma_p \pi}} \quad (2)$$

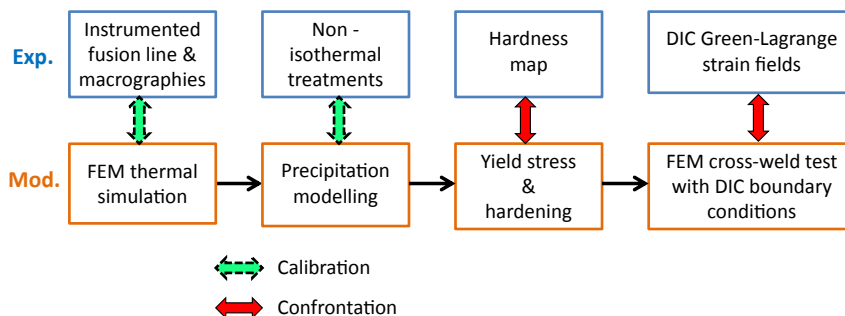


Fig. 4. Modelling (mod.) strategy and link with experimental (exp.) investigations.

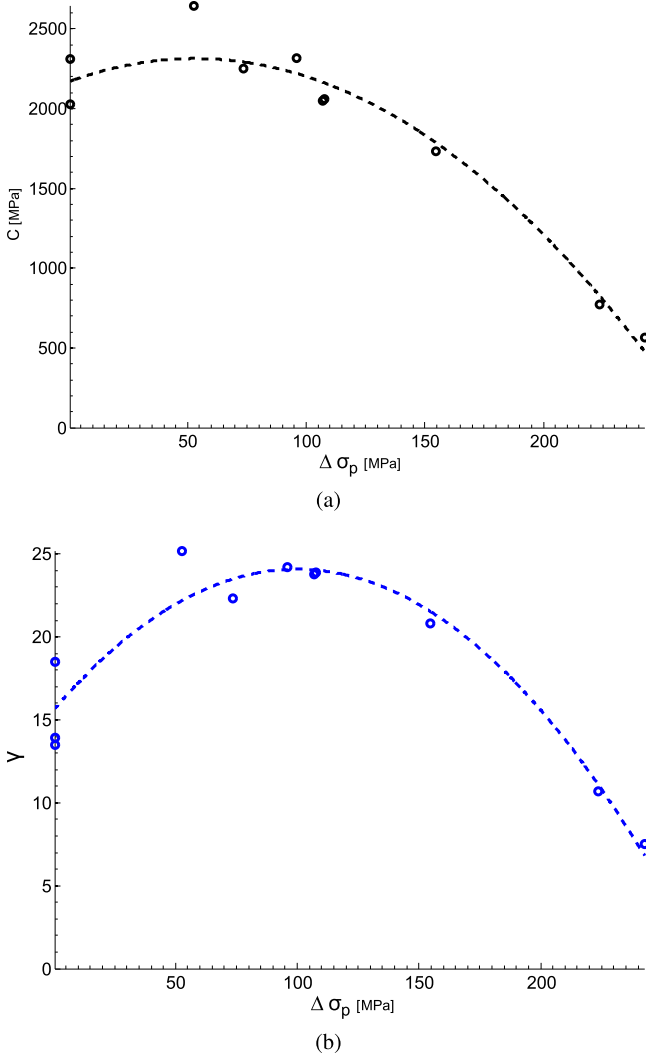


Fig. 6. The two master curves deduced from the work hardening fitting used after non-isothermal heat treatments for the Armstrong-Frederick model. The parameter C (a) and γ (b) are plotted and as function of the precipitate hardening contribution $\Delta\sigma_p$.

In this expression, 2ξ , k_B , γ_p and Δg are respectively the aspect ratio of the precipitate, the Boltzmann constant, the surface energy and the driving force (function of the solubility product K_s) at temperature T . These two last (K_s , γ_p) were calibrated thanks to the Small Angle Neutrons Scattering (SANS) experimental data and the Transmission Electron Microscopy (TEM) characterisations [9].

Afterwards, the length (l_i) increment for needle precipitates of the class 'i' is:

$$\frac{dl_i}{dt} = 1.5 \frac{D_{Mg}}{2r_i} \frac{X_{Mg} - X_{Mg}^i}{\alpha X_{Mg}^p - X_{Mg}^i} = 1.5 \frac{D_{Si}}{2r_i} \frac{X_{Si} - X_{Si}^i}{\alpha X_{Si}^p - X_{Si}^i} \quad (3)$$

where D_k is the diffusion coefficient of element k ; X_{Mg} and X_{Si} are the matrix solute fraction; X_{Mg}^i and X_{Si}^i are the interfacial equilibrium solute fraction; α is the ratio between matrix and precipitate mean atomic volume v_{at} ($\alpha = v_{at}^M/v_{at}^p$); $X_{Mg}^p = x/(x+y)$ and $X_{Si}^p = y/(x+y)$ are the precipitate solute fraction of a precipitate Mg_xSi_y . The Gibbs-Thomson effect, which describes the precipitate size effect on its stability, is coupled to the growth equation (3) as in Ref. [9]:

$$X_{Mg}^i X_{Si}^i = K_s \cdot \exp\left(\frac{4\xi\gamma_p v_{at}^p (x+y)}{r(3\xi-2)k_b T}\right) \quad (4)$$

Finally, the mass balance allows the solute fraction available in solid solution to be updated, thanks to the precipitation volume fraction f_v in the unit volume:

$$X_i = \frac{X_i^{ini}[1 + \alpha f_v - f_v] - X_i^p \alpha f_v}{1 - f_v} \quad (5)$$

The parameters of this model are provided in a previous work [9]. By coupling all these equations (eq. (1) to eq. (5)) and using a resolution scheme described in Refs. [23], the precipitate distribution can be determined in each element corresponding to a given temperature history.

3.3. Yield stress prediction

Knowing the precipitate distribution and the atomic fraction of solute elements in the mesh, a microstructure-based yield stress model can be used (see Ref. [9]). It is composed of several contributions to the yield stress namely: the solid solution $\Delta\tau_{SS}$, the grain boundaries $\Delta\tau_{gb}$, the precipitates $\Delta\tau_p$ and dislocations $\Delta\tau_d$ contributions. These contributions are homogenised in the slip planes thanks to conventional power laws, $\Delta\tau_{tot}^k = \sum_i \Delta\tau_i^k$, where k is dependent on the difference in size and strength of obstacles for the contributions $\Delta\tau_i$ [24]. This total hardening is added to the friction stress of pure aluminium τ_0 . Starink et al. [25] have shown that the grain size contribution is in most cases negligible in comparison to precipitation. This effect is only taken into account here by introducing the initial yield stress of a pure aluminium $\sigma_0 = 10$ MPa [26]. The forest hardening $\Delta\tau_d$ has an important effect on the plastic behaviour of 6061 alloys [14] but, for moderate preformed alloys, this contribution has a weak impact on the initial yield stress [14,27]. So, by assuming a constant mean Taylor's factor (M), the macroscopic yield stress can be described as [14]:

$$\sigma_y = \sigma_0 + R = \sigma_0 + \Delta\sigma_{SS} + \sqrt{\Delta\sigma_p^2 + \Delta\sigma_d^2} \approx \sigma_0 + \Delta\sigma_{SS} + \Delta\sigma_p \quad (6)$$

where R is the isotropic contribution. According to the thermal finite element simulation (Fig. 8), the solid solution $\Delta\sigma_{SS} = \sum_j k_j \cdot X_{wt}^{j2/3}$ and precipitate $\Delta\sigma_p = \sqrt{\Delta\sigma_{sh}^2 + \Delta\sigma_{bp}^2}$ strengthening contributions are updated according to [9]:

$$\begin{cases} \Delta\sigma^{sh} = M \left(\frac{2\beta b \mu}{r_c}\right)^{3/2} \sqrt{\frac{\sum_{i < l_c} l_i N_i}{4\sqrt{3}\beta \mu b} \left[\frac{\sum_{i < l_c} N_i r_i}{\sum_{i < l_c} N_i}\right]^{3/2}} \\ \Delta\sigma^{bp} = \sqrt{2} M \beta \mu b \sqrt{\sum_{i > l_c} l_i N_i} \end{cases} \quad (7)$$

where σ_{bp} and σ_{sh} are the expressions for the by-passed and sheared precipitates and μ , b , r_c , β , k_j , X_{wt}^j are, respectively, the shear modulus, the Burgers's vector, the transition radius between the shearing and by-passing precipitate/dislocation interactions [28], the line tension constant and the strengthening constant associated with the weight fraction of solutes in solution.

3.4. Work hardening model

To reproduce the experimental tensile data shown in Fig. 5, a work hardening model is used. For this kind of aluminium alloys

the work hardening is commonly assumed to be isotropic [6,7] because they are based on monotonous tensile tests. However, other contributions affect the elasto-plastic behaviour of aluminium [14]: (i) the grain boundaries produce a non negligible kinematic hardening X , (ii) the dislocation density evolution increases the total isotropic contribution R , and (iii) precipitates affect the isotropic contributions through the slip resistance $\Delta\sigma_p$ as well as the kinematic hardening.

In a previous study [14], cyclic tests performed on the T6 state (fully precipitated state) demonstrated that no isotropic work hardening occurs because the forest hardening $\Delta\sigma_d$ term is negligible compared to the precipitate contribution $\Delta\sigma_p$. During the coarsening/dissolution, this contribution $\Delta\sigma_d$ increases but its evolution is assumed negligible here. So, for the sake of simplicity, it was chosen here to model the elasto-plastic behaviour through two contributions: (i) a constant isotropic hardening due to solute and precipitates, and (ii) a kinematic hardening X due to microstructural interactions (such as grain boundaries and precipitates):

$$\begin{cases} R = \Delta\sigma_{SS} + \Delta\sigma_p \\ \frac{\partial n}{\partial \varepsilon_p} = \gamma \cdot n^* \left(1 - \frac{n}{n^* \cdot \text{Sign}(\varepsilon_p)} \right) \\ X = \frac{C}{\gamma} \frac{n}{n^*} \end{cases} \quad (8)$$

where γ is the recall term (dynamic recovery, as defined by Chaboche [29]) and C is given by: $\dot{X} = C\dot{\varepsilon}_p$, in the absence of recovery. The term n is the number of dislocations interacting with defects (precipitates or grain boundaries) and n^* is the saturation value of n [14].

Deriving previous equation (8) leads to the classical form of the 1D Armstrong-Frederick relation [14]:

$$\dot{X} = C\dot{\varepsilon}_p - \gamma X \dot{p} \quad (9)$$

where p is the cumulative plastic deformation. Bardel et al. [14] showed that the parameters γ and C of the Armstrong-Frederick relation were related to the microstructure (precipitation state and/or grain size). In this paper, we will then assume that γ and C are functions of $\Delta\sigma_p$, the precipitates contribution to the hardening, which represent here the contribution of the microstructure to hardening. First, γ and C will be used as fitting parameters to describe tensile tests performed on all microstructural states. Then, these two parameters will be expressed as a function of $\Delta\sigma_p$ (see eq. (12)).

In order to provide a 3D constitutive law that is further used in FEM, the previous description of plasticity should be described in a tensorial form. As no texture was observed in these samples [13], isotropic plasticity has been assumed, leading to:

$$\underline{\dot{X}} = \frac{2}{3} C \dot{\varepsilon}_p - \gamma \cdot \underline{X} \cdot \dot{p} \quad (10)$$

where the cumulative plastic strain rate is: $\dot{p} = \sqrt{\frac{2}{3} \dot{\varepsilon}_p : \dot{\varepsilon}_p}$

The general constitutive set of equations can thus be written as:

$$\begin{cases} \dot{\underline{\sigma}} = \underline{C} (\dot{\underline{\varepsilon}} - \dot{\varepsilon}_p \underline{p}) \\ \dot{\varepsilon}_p = \dot{\lambda} \frac{\partial f}{\partial \underline{\sigma}} \\ f = J_2 (\underline{\sigma} - \underline{X}) - (\sigma_0 + R) \\ R = \Delta\sigma_{SS} + \Delta\sigma_p \\ \underline{\dot{X}} = \frac{2}{3} C \dot{\varepsilon}_p - \gamma \underline{X} \dot{p} \\ \dot{\lambda} = \dot{p} \end{cases} \quad (11)$$

where C is the elastic constants tensor, f is the yield function, λ is the plastic multiplier and J_2 is the second deviatoric stress invariant.

Fig. 5 represents the tensile tests performed on all specimens corresponding to all investigated microstructures. As mentioned earlier, these curves have been fitted according to the elasto-plastic formalism derived in the set of eq. (11) with γ and C being the only fitting parameters. Note that the excellent agreement validates the Armstrong-Frederick formalism used here. The result of the fit is given in Fig. 6, where γ and C are represented as a function of $\Delta\sigma_p$, each point corresponding to a given microstructure. It can be seen that both $\gamma(\sigma_p)$ and $C(\sigma_p)$ can be relatively well described by second degree polynomial functions:

$$\begin{cases} \gamma = -847.8 \times 10^{-6} \Delta\sigma_p^2 + 0.1695 \Delta\sigma_p + 15.61 \\ C = -5122 \times 10^{-5} \Delta\sigma_p^2 + 5.456 \Delta\sigma_p + 2168 \end{cases} \quad (12)$$

Thanks to this semi-phenomenologic approach, two effects discussed in Ref. [14] were well captured (Fig. 6): (i) the reduction of the hardening modulus with increasing precipitate contribution $\Delta\sigma_p$ and (ii) the increase in the work hardening saturation for the overaged states (intermediate values of $\Delta\sigma$ [9]) thanks to the precipitate-induced cross-slip mechanism [7]. This model can be then applied on the cross-weld mechanical test.

4. Finite element simulation

4.1. Thermal simulation

To simulate a tensile cross-weld test is to simulate the thermal history in the structure during welding. To achieve this goal, an equivalent heat source approach was used to replace the complex multi-physic problem by a nonlinear conduction resolution [18], the problem becomes:

$$\rho(T) C_p(T) \frac{\partial T}{\partial t} - \nabla \cdot (\lambda(T) \nabla T) - Q_i = 0 \quad (13)$$

where ρ , C_p , λ and Q_i are the density [$\text{kg} \cdot \text{m}^{-3}$], the heat capacity [$\text{J} \cdot \text{Kg}^{-1} \text{K}^{-1}$], the thermal conductivity [$\text{W} \cdot \text{m}^{-1} \text{K}^{-1}$] and an equivalent internal heat source [$\text{W} \cdot \text{m}^{-3}$] that has been calibrated using K-type thermocouples measurements [13]. Due to symmetry, this FE model has been applied on a half plate (Fig. 8) with a high density of hexahedral 8-nodes and some linear prismatic 6-node elements in the area of interest (the numerical tensile specimen) and a low density in the rest of the geometry (Fig. 7). The tensile specimen introduced in the meshed plate (Fig. 7) is used to perform the tensile cross-weld test after the thermal finite element simulation. As the electron beam welding process induces high thermal

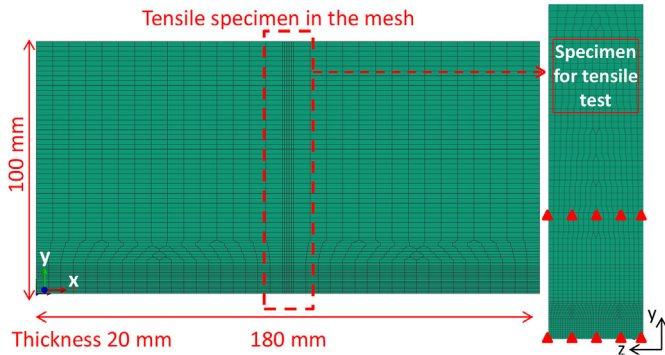


Fig. 7. Mesh used for the thermal computation and numerical specimen extracted from the global mesh for the tensile cross-weld test. Triangles on the right mesh mark the position of the displacement boundary condition coming from the DIC.

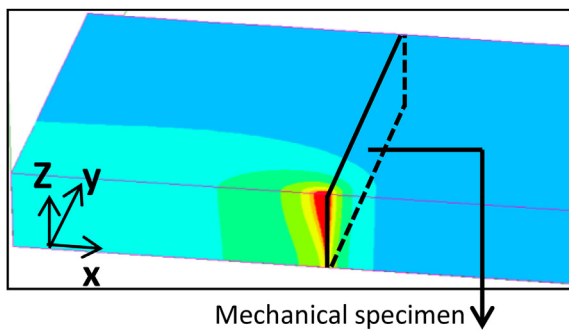


Fig. 8. Representation of the calibrated FE thermal model of a fusion line process for a 6061-T6 aluminium plate (half plate is presented because of symmetry) [13].

gradients, a high mesh density was used close to the molten zone and a progressive reduction was used. The mesh comprised 74,569 elements and 67,614 nodes. The dimensions of the smallest element were $0.8 \times 0.5 \times 0.5 \text{ mm}^3$ (x,y,z) in the molten zone. The tensile mesh had 7855 elements and 9798 nodes.

In this paper, the calibration of the FE thermal simulation is not presented (all details are in Ref. [13]). Nevertheless, the thermal FE simulation of the welding process is shown and confronted to an experimental macrography on Fig. 1.

4.2. Microstructural evolution

To simulate the microstructural evolution in this semi-section, certain information had to be provided to our microstructural software ('nodePreciSo'), such as the thermodynamic and crystallographic data of the alloy (here 6061), its hardening β' - β' phases and its initial precipitate size distribution for the T6 state. The microstructural results, in terms of volume fraction and average radius, for this 6061-T6 aluminium alloy subjected to welding treatment are presented in Fig. 10 for a semi-section. In Fig. 9, the atomic fraction of the main alloying elements (Mg and Si) are presented and show the increase of the solute content close to the weld when β' - β' precipitates coarsen or dissolve.

4.3. Hardness results

Thanks to the multi-class approach, the thermo-microstructural simulations provide a good representation of the precipitation state for highly anisothermal treatments [9]. The precipitate modelling can then be coupled to the strengthening model presented in eq. (6), and the Vickers hardness (HV) can be approximated thanks to a

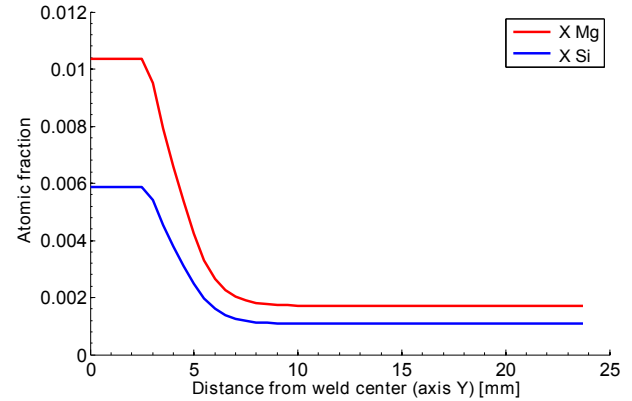


Fig. 9. The increase in atomic fraction of magnesium and silicon across the weld due to precipitate dissolution (profile for the mid-thickness).

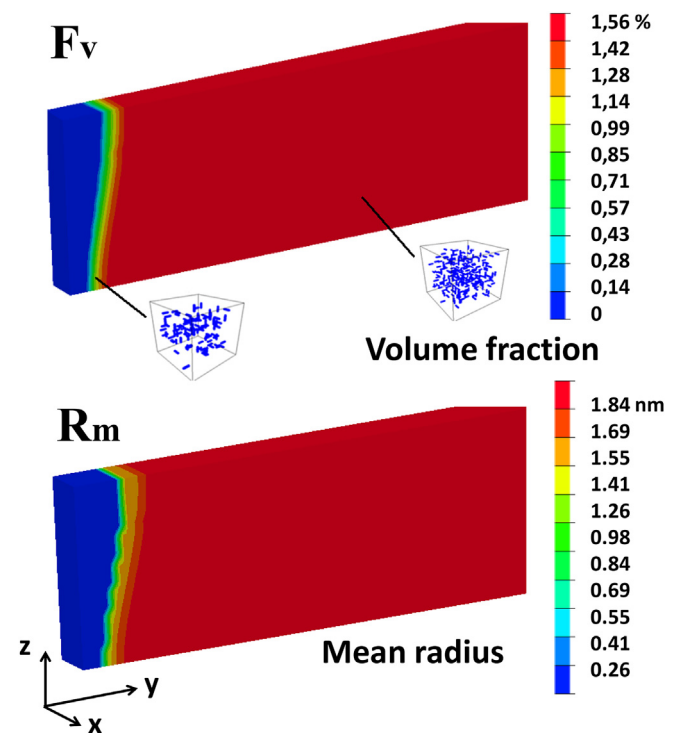


Fig. 10. Microstructural field provided by the finite element simulations, the volume fraction F_v and the mean radius R_m of the distribution.

linear interpolation [7,30–32]:

$$HV = A_{HV} \cdot \sigma_y + B_{HV} = 0,24 \cdot \sigma_y + 48.5 \quad (14)$$

where A_{HV} and B_{HV} have been identified by the comparison between tensile tests for the T6 and the SSS state and two corresponding hardness points.

The model has been applied on the weld section and comparisons are shown in Figs. 11 and 12. It is shown that the metallurgical modelling coupled with the thermal finite element histories approximates the hardness fairly well after the electron beam welding process.

4.4. Cross-weld tensile results

The precipitation-yield stress model, previously calibrated on

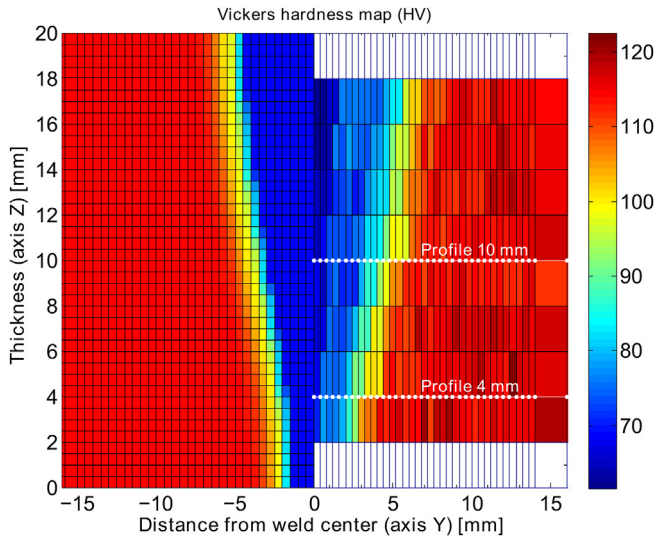


Fig. 11. Confrontation between the numerical (left) and experimental (right) hardness maps. The colour of each element is the average of the hardness measurements performed on each node. (For interpretation of the references to colour in this figure caption, the reader is referred to the web version of this article.)

representative non-isothermal heat treatments, was coupled to the thermal FE simulation. First, before the thermal computation, a T6 precipitation state was generated from an 8-h treatment at 175 °C [9] and assigned to each mesh. Next, during each time step, the evolution of the precipitate distribution was computed and the hardening yield stress components $\Delta\sigma_{SS}$, $\Delta\sigma_p$ and work hardening constants were updated.

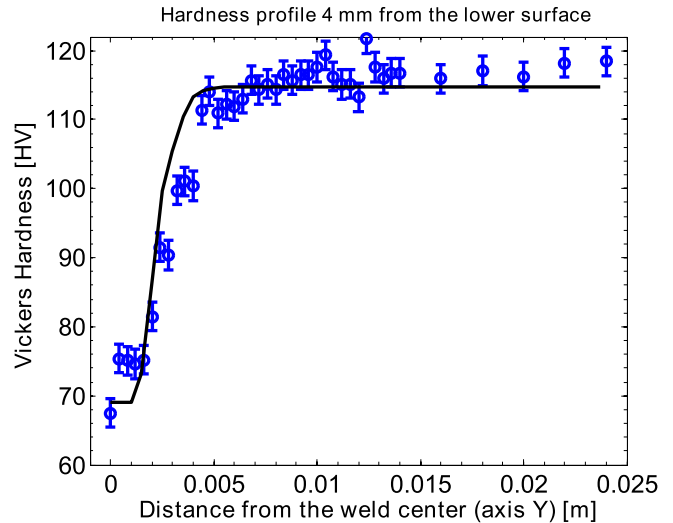
After the thermal simulation, the microstructural state and, therefore, the constitutive laws were known in each integration point, as shown in Fig. 10, the numerical cross-weld tensile test could be performed by applying a global displacement. To avoid any idealisation in the boundary conditions, the experimental displacements from the DIC experiments (Figs. 2 and 3) were imposed to the mesh represented in Fig. 7 and a large strain computation was performed. Note that the residual stresses, previously developed during the fusion line treatment, were neglected here in view of the thin thickness of the sample (a total relaxation is assumed).

The results of this mechanical simulation are shown in Fig. 13. In these results, a confrontation between the numerical and experimental Green-Lagrange (E) strain maps show a very good agreement and validate this methodology to reproduce heterogeneous structural behaviour.

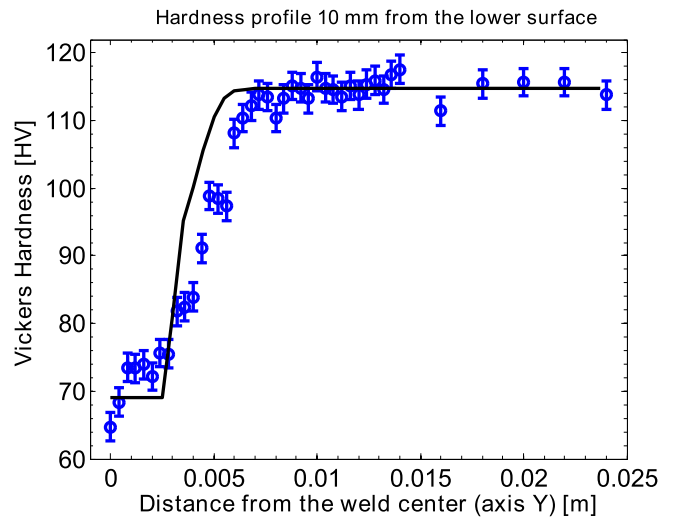
Once the global strain response was validated, the stress field was then provided by the finite element software, as shown in Fig. 14a with the von Mises stress field. The concentration of the equivalent stress was located between the molten and the heat affected zones, which was consistent with the maximum shear strain gradient observed in DIC experiments (Fig. 2). In Fig. 14b, the post-tensile von Mises stresses were also represented to highlight where the plastic strain gradients could be located during the tensile test.

5. Discussion

As previously mentioned, a coupled microstructural-mechanical model was calibrated in order to reproduce the constitutive behaviour of the 6061-T6 alloy for several anisothermal treatments. This semi-phenomenological method is able to predict the strain field encountered across a weld joint. The most important



(a)



(b)

Fig. 12. Confrontation between experimental and numerical hardness lines for a distance of 4 mm (a) and 10 mm (b) from the lower surface.

assumptions are:

- The isotropic hardening is accounted for only for the initial yield stress, through the strength increments $\Delta\sigma_p$ and $\Delta\sigma_{SS}$ that are not linked to the work-hardening. For cyclic loading, the description of the mechanical behaviour will be less accurate in the molten zone since an isotropic work-hardening contribution can take place. This approximation is also limiting for the physical interpretation of the hardening constants presented in this work. This is why this approach is named semi-phenomenological. For more complex loading cycles, it would be necessary to account for kinematic hardening with a finer description of internal variables.
- The microstructural simulation is limited to the hardening phase $\beta''-\beta'$. A more accurate description could be proposed in order to predict the distribution of each phase separately.
- The Guinier-Preston zones, which nucleate during natural ageing, are not accounted for. For the presented experiments, this phenomenon was limited by preventing ageing of the material before the cross-weld tensile test. Nevertheless, in

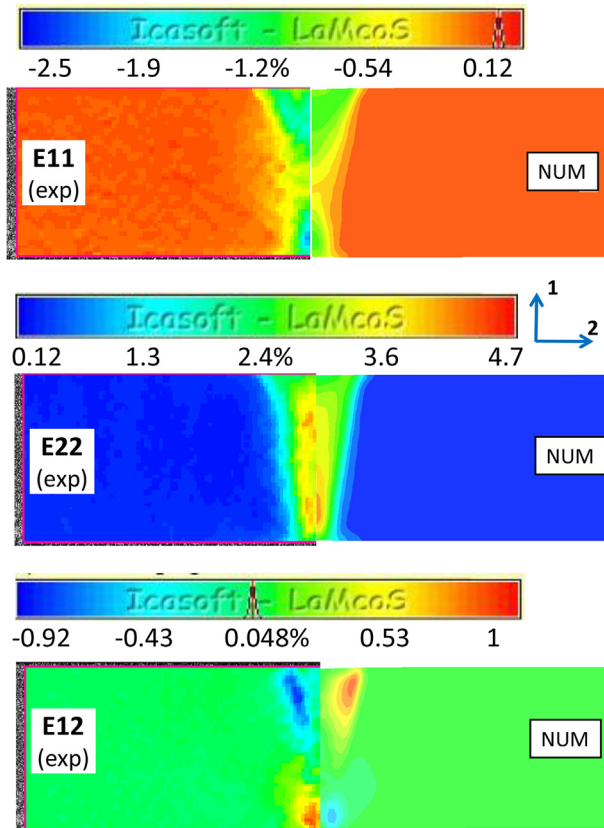


Fig. 13. Confrontation between experimental (exp) and numerical (num) Green-Lagrange strain components (E). The experimental results presented in Fig. 3 are well reproduced.

practical applications, an additional age-hardening contribution can arise in the molten zone. The current model, therefore, underestimates the hardening in this zone.

By considering these assumptions as acceptable, this model can be used for industrial applications and may provide a good approximation of the behaviour of welded structures. The application to cyclic loadings should be considered with care since the kinematic/isotropic hardening ratio could evolve with the degradation of the alloy [14]. The prediction for cyclic loadings would be thus gradually less accurate closer to the weld center with a good prediction of the T6 state.

6. Conclusion

A 6061-T6 aluminium sheet was subjected to a fusion line treatment in order to get a heterogeneous structure in terms of precipitation state. Then, a cross-weld tensile experiment was conducted and analysed by DIC to understand the distribution of the strain components in the various weld zones for tensile loading.

In order to reproduce this experiment numerically, two finite element analyses were performed. First, a thermal fusion line computation was used to know the thermal history in the whole plate (which contains the tensile specimen). Next, thanks to a coupling between the finite element software (SYSWELD) and a recently developed precipitation model, the microstructural state in the structure and, consequently, the mechanical properties for each integration point before the mechanical testing were deduced.

The semi-phenomenologic microstructure informed law,

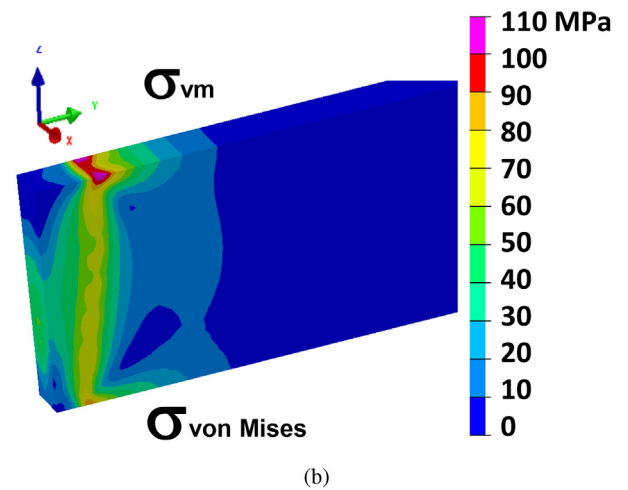
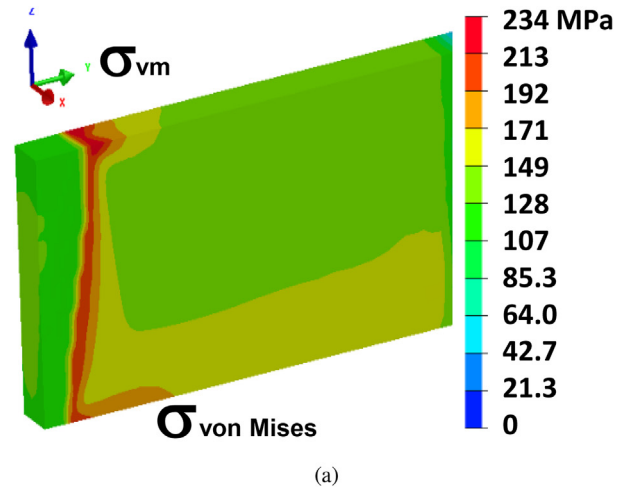


Fig. 14. Representation of von Mises stresses (a) at the end of the tensile test (displacement equal to 2 mm) and (b) after the tensile test. The half specimen is presented because of the geometry.

proposed in this paper, was only calibrated on the classical tensile test performed after representative heat treatments. Nevertheless the numerical cross-weld simulation provides very good predictions of global strain fields as highlighted by the DIC experiments. Therefore, the proposed approach provides high accuracy predictions of the residual microstructural state and material properties in welded structures.

Acknowledgements

The authors gratefully acknowledge AREVA, France and the French Atomic Energy Commission (CEA) for their industrial and financial support. We would also like to thank Frederic Boitout from the ESI Group for his technical help on SYSWELD. D.B. wants to acknowledge M. Zain-UI-Abdein for the fruitful discussions on welding, and F. Morestin for providing the Icasoft software.

Nomenclature

N_i	number density precipitate in class i [$\# \text{ m}^{-3}$]
Z	Zeldovich factor
N_0	number of nucleation sites per unit volume
T	temperature [K] or [$^{\circ}\text{C}$]

β^*	condensation rate
ΔG^*	Gibbs energy change for the formation of a critical nucleus [J]
k_b	Boltzmann constant [J/K]
τ	incubation time
r_{kBT}^*	stable critical radius of nucleation [m]
δg	driving force of nucleation [J m ⁻³]
γ_p	precipitate/matrix interface energy [J m ⁻²]
K_s	solubility product of the hardening phase
ξ	semi aspect ratio of the hardening phase
l_i	length of precipitate of class i [m]
$\frac{dl}{dt}$	precipitate growth rate [m s ⁻¹]
D_k	diffusion coefficient of element k [m ² s ⁻¹]
r_i	radius of precipitate in the class i [m]
α	ratio of atomic volume between matrix and precipitate
X_i^{ini}	initial atomic fraction for element i in the matrix
X_i	atomic fraction for element i in the matrix
X_i^i	atomic fraction of i element at the interface between matrix and precipitate
X_i^p	atomic fraction of i element in the precipitate
x, y	chemical coefficients for the precipitates
v_{at}^M	mean atomic volume of the matrix [m ³]
v_{at}^p	precipitate mean atomic volume [m ³]
f_v	volume fraction of the precipitates
$\Delta\tau_d, \Delta\sigma_d$	dislocation contribution to strength [MPa]
$\Delta\tau_p, \Delta\sigma_p$	precipitate contribution to strength [MPa]
$\Delta\tau_p, \Delta\sigma_p$	precipitate contribution to strength [MPa]
$\Delta\tau_{SS}, \Delta\sigma_{SS}$	solid solution contribution to strength [MPa]
$\Delta\tau_{gb}$	grain contribution to strength [MPa]
σ_y	engineering yield stress [MPa]
σ_0	pure aluminium yield stress [MPa]
$\Delta\sigma^{bp}$	by-passed precipitates contribution to yield stress [MPa]
$\Delta\sigma^{sh}$	sheared precipitates contribution to yield stress [MPa]
M	Taylor factor
k_i	constant for solid solution strengthening for element 'i'.
X_{wt}^j	weight percent fraction of element j in the matrix
r_i	precipitate radius for the class 'i' [m]
r^c	critical radius for the shearing/by-passing transition [m]
b	Burgers vector [m]
β	dislocation line tension
μ	aluminium shear modulus [MPa]
X	Armstrong-Frederick hardening variable [MPa]
C	first constant of the Armstrong-Frederick model [MPa]
γ	second constant of the Armstrong-Frederick model
p	cumulative plastic strain
ρ	volumic density [kg m ⁻³]
C_p	massic capacity [J kg ⁻¹ K ⁻¹]
λ	thermal conductivity [W m ⁻¹ K ⁻¹]
Q_i	internal heat source [W m ⁻³]

References

- [1] D. Lassance, D. Fabregue, F. Delannay, T. Pardoën, Micromechanics of room and high temperature fracture in 6xxx al alloys, *Prog. Mater. Sci.* 52 (2007) 62–129.
- [2] D. Fabregue, T. Pardoën, A constitutive model for elastoplastic solids containing primary and secondary voids, *J. Mech. Phys. Solids* 56 (2008) 719–741.
- [3] J. Andersen, H.W. Zandbergen, J. Jansen, C. Traeholt, U. Tundal, O. Reiso, The crystal structure of the β' phase in Al-Mg-Si alloys, *Acta Mater.* 46 (1998) 3283–3298.
- [4] J. Lipkin, J. Swearingen, C. Karnes, Mechanical properties of 6061 al-mg-si alloy after very rapid heating, *J. Mech. Phys. Solids* 21 (1973) 91–112.
- [5] O. Grong, H. Shercliff, Microstructural modelling in metals processing, *Prog. Mater. Sci.* 47 (2002) 163–282.
- [6] K. Nielsen, T. Pardoën, V. Tvergaard, B. de Meester, A. Simar, Modelling of plastic flow localisation and damage development in friction stir welded 6005a aluminium alloy using physics based strain hardening law, *Int. J. Solids Struct.* 47 (2010) 2359–2370.
- [7] A. Simar, Y. Bréchet, B. de Meester, A. Denquin, C. Gallais, T. Pardoën, Integrated modeling of friction stir welding of 6xxx series Al alloys: process, microstructure and properties, *Prog. Mater. Sci.* 57 (2012) 95–183.
- [8] O. Myhr, O. Grong, H. Fjaer, C. Marioara, Modelling of the microstructure and strength evolution in Al-Mg-Si alloys during multistage thermal processing, *Acta Mater.* 52 (2004) 4997–5008.
- [9] D. Bardel, M. Perez, D. Nelias, A. Deschamps, C. Hutchinson, D. Maisonnette, T. Chaise, J. Garnier, F. Bourlier, Coupled precipitation and yield strength modelling for non-isothermal treatments of a 6061 aluminium alloy, *Acta Mater.* 62 (2014) 129–140.
- [10] Q. Puydt, S. Flouriot, S. Ringeval, F.D. Geuser, R. Estevez, G. Parry, A. Deschamps, Relationship between microstructure, strength, and fracture in an al-zn-mg electron beam weld: Part ii: mechanical characterization and modeling, *Metallurgical Mater. Trans. A* 45A (2014) 6141–6152.
- [11] O. Myhr, O. Grong, Process modelling applied to 6082-t6 aluminium weldments-i. reaction kinetics, *Acta Metallurgica Materialia* 39 (1991), 2963–2702.
- [12] A. Hirose, K. Kobayashi, H. Yamaoka, N. Kurosawa, Evaluation of properties in laser welds of A6061-T6 aluminium alloy, *Weld. Int.* 14 (6) (2000) 431–438.
- [13] D. Bardel, D. Nelias, V. Robin, T. Pirling, X. Boulmat, M. Perez, Residual stresses induced by electron beam welding in a 6061 aluminium alloy, *J. Mater. Process. Technol.* 235 (2016) 1–12.
- [14] D. Bardel, M. Perez, D. Nelias, S. Dancette, P. Chaudet, V. Massardier, Cyclic behaviour of a 6061 aluminium alloy: coupling precipitation and elastoplastic modelling, *Acta Mater.* 83 (2015) 256–268.
- [15] M. Nicolas, A. Deschamps, Characterisation and modelling of precipitate evolution in an Al-Zn-Mg alloy during non-isothermal heat treatments, *Acta Mater.* 51 (2003) 6077–6094.
- [16] R. Kampmann, R. Wagner, Decomposition of alloys: the early stages, in: *Kinetics of Precipitation in Metastable Binary Alloys – Theory and Application to Cu-1.9 at% Ti and Ni-14 at% Al*, Pergamon Press, 1984, pp. 91–103.
- [17] J. Goldak, A. Chakravati, M. Bibby, A new finite element model for welding heat sources, *Metall. Trans.* 15B (1984) 299–305.
- [18] M. Zain-UI-Abdein, D. Nelias, J. Jullien, D. Deloison, Prediction of laser beam welding-induced distortions and residual stresses by numerical simulation for aeronautic application, *J. Mater. Process. Technol.* 209 (2009) 2907–2917.
- [19] Sysweld, User's Reference Manual, ESI Group, 2014.
- [20] T. Mabrouki, J.-F. Rigal, A contribution to a qualitative understanding of thermo-mechanical effects during chip formation in hard turning, *J. Mater. Process. Technol.* 176 (2006) 214–221.
- [21] L. Delannay, O. Mishin, Crystal plasticity modeling of the through-thickness texture heterogeneity in heavily rolled aluminum, *Key Eng. Mater.* 554 (2013) 1189–1194.
- [22] S. Mguil-Touchal, F. Morestin, M. Brunet, Various experimental applications of digital image correlation method, *CMEM Rhodes* 97 (1997) 45–58.
- [23] M. Perez, M. Dumont, D. Acevedo-Reyes, Implementation of classical nucleation and growth theories for precipitation, *Acta Mater.* 56 (2008) 2119–2132.
- [24] S. Queyreau, G. Monnet, B. Devincere, Orwan strengthening and forest hardening superposition examined by dislocation dynamics simulations, *Acta Mater.* 58 (2010) 5586–5595.
- [25] M. Starink, A. Deschamps, S. Wang, The strength of friction stir welded and friction stir processed aluminium alloys, *Scr. Mater.* 58 (2008) 377–382.
- [26] A. Deschamps, Y. Bréchet, Influence of predeformation and ageing of Al-Zn-Mg alloy-II. Modeling of precipitation kinetics and yield stress, *Acta Mater.* 47 (1999) 293–305.
- [27] G. Fribourg, Y. Bréchet, A. Deschamps, A. Simar, Microstructure-based modelling of isotropic and kinematic strain hardening in a precipitation-hardened aluminium alloy, *Acta Mater.* 59 (2011) 3621–3635.
- [28] A. Takahashi, N.M. Ghoniem, A computational method for dislocation-precipitate interaction, *J. Mech. Phys. Solids* 56 (2008) 1534–1553.
- [29] J. Chaboche, A review of some plasticity and viscoplasticity constitutive theories, *Int. J. Plasticity* 24 (2008) 1642–1693.
- [30] N. Kamp, A. Sullivan, J. Robson, Modelling of friction stir welding of 7xxx aluminium alloys, *Material Sci. Eng. A* 46624 (2007) 6–255.
- [31] O. Myhr, O. Grong, S. Andersen, Modelling of the age hardening behaviour of Al-Mg-Si alloys, *Acta Mater.* 49 (2001) 65–75.
- [32] C. Gallais, A. Denquina, Y. Bréchet, G. Lapasset, Precipitation microstructures in an AA6056 aluminium alloy after friction stir welding : characterisation and modelling, *Mater. Sci. Eng. A* 496 (2008) 77–89.